The Astrophysical Journal, 686:851–858, 2008 October 20

A MOLECULAR EINSTEIN RING AT $z = 4.12$: IMAGING THE DYNAMICS OF A QUASAR HOST GALAXY THROUGH A COSMIC LENS

Dominik A. Riechers,[1,2,3] Fabian Walter,[1] Brendon J. Brewer,[4] Christopher L. Carilli,[5] Geraint F. Lewis,[4] Frank Bertoldi,[6] and Pierre Cox[7]

Received 2007 December 22; accepted 2008 June 27

ABSTRACT

We present high-resolution (0.3″) Very Large Array imaging of the molecular gas in the host galaxy of the high-redshift quasar PSS J2322+1944 ($z = 4.12$). These observations confirm that the molecular gas (CO) in the host galaxy of this quasar is lensed into a full Einstein ring and reveal the internal gas dynamics in this system. The ring has a diameter of ∼1.5″ and thus is sampled over ∼20 resolution elements by our observations. Through a model-based lens inversion, we recover the velocity gradient of the molecular reservoir in the quasar host galaxy of PSS J2322+1944. The Einstein ring lens configuration enables us to zoom in on the emission and to resolve scales down to ≲1 kpc. From the model-reconstructed source, we find that the molecular gas is distributed on a scale of 5 kpc and has a total mass of $M(\mathrm{H_2}) = 1.7 \times 10^{10}\,M_\odot$. A basic estimate of the dynamical mass gives $M_{\rm dyn} = 4.4 \times 10^{10}\,\sin^{-2} i\,M_\odot$, that is, only ∼2.5 times the molecular gas mass and ∼30 times the black hole mass (assuming that the dynamical structure is highly inclined). The lens configuration also allows us to tie the optical emission to the molecular gas emission, which suggests that the active galactic nucleus does reside within, but not close to the center of, the molecular reservoir. Together with the (at least partially) disturbed structure of the CO, this suggests that the system is interacting. Such interaction, possibly caused by a major "wet" merger, may be responsible for both feeding the quasar and fueling the massive starburst of 680 $M_\odot\,\mathrm{yr}^{-1}$ in this system, in agreement with recently suggested scenarios of quasar activity and galaxy assembly in the early universe.

Subject headings: cosmology: observations — galaxies: active — galaxies: formation — galaxies: high-redshift — galaxies: starburst — radio lines: galaxies

Online material: color figure

1. INTRODUCTION

A fundamental aspect in studies of galaxy formation and evolution is to understand the connection between active galactic nucleus (AGN) and starburst activity. The existence of a physical connection between both processes is suggested by the finding that present-day galaxies show a strong relationship between the mass of their central supermassive black holes (SMBHs) and the mass and concentration of their stellar spheroids (Magorrian et al. 1998; Ferrarese & Merritt 2000; Gebhardt et al. 2000; Graham et al. 2001). If these relations were due to a coevolution of both components during the early assembly of a galaxy, high-redshift quasars and their associated host galaxies would be ideal objects to study the active formation of both SMBHs and bulge stars.

Studies of molecular gas (most commonly rotational transitions of CO), the prerequisite material that fuels star formation, have become an important tool to probe distant quasar host galaxies and revealed large molecular gas reservoirs of $>10^{10}\,M_\odot$ in a number of these sources (see Solomon & Vanden Bout 2005 for a general review). These galaxies typically show huge far-infrared (FIR) luminosities in excess of $10^{13}\,L_\odot$, which are thought to be powered by starbursts (and possibly a central AGN; e.g., Omont et al. 2001; Wang et al. 2008). Observations of molecular gas trace the regions that can host massive starbursts. In addition, the velocity structure of molecular line emission has the potential to constrain the dynamical state of galaxies out to the earliest epochs.

Rotational molecular line emission typically emerges at FIR to radio wavelengths, i.e., in the limited wavelength regime where the AGN in distant quasars does not outshine all other emission. However, the cosmological distances of high-redshift quasars make it difficult to resolve the faint emission from their host galaxies at such long wavelengths. The physical resolution of such observations is in some cases boosted by gravitational lenses acting as natural telescopes. The gravitational lensing effect also magnifies the observed flux of the background galaxy, in particular for systems in Einstein ring configurations. Due to the compactness of the AGN, optical quasars in Einstein ring lens configurations are rare. Due to their greater extent, the host galaxies of quasars are much more likely to cross the inner Einstein ring caustic of a gravitational lens.

In this paper, we report on high (0.3″) angular resolution Very Large Array (VLA)[8] observations of CO in the host galaxy of the $z = 4.12$ quasar PSS J2322+1944, one of only two known $z > 4$ galaxies that are both gravitationally lensed and detected in molecular gas emission (the other being BRI 0952−0115 at $z = 4.43$; Guilloteau et al. 1999). This galaxy was identified in a spectroscopic follow-up study of the Palomar Sky Survey (DPOSS;

[1] Max-Planck-Institut für Astronomie, Königstuhl 17, Heidelberg, D-69117, Germany.
[2] Astronomy Department, California Institute of Technology, MC 105-24, 1200 East California Boulevard, Pasadena, CA 91125.
[3] Hubble Fellow.
[4] Institute of Astronomy, School of Physics, A28, University of Sydney, NSW 2006, Australia.
[5] National Radio Astronomy Observatory, P.O. Box O, Socorro, NM 87801.
[6] Argelander-Institut für Astronomie, Universität Bonn, Auf dem Hügel 71, Bonn, D-53121, Germany.
[7] Institut de RadioAstronomie Millimétrique, 300 Rue de la Piscine, Domaine Universitaire, F-38406 Saint Martin d'Hères, France.

[8] The Very Large Array is a facility of the National Radio Astronomy Observatory, operated by Associated Universities, Inc., under a cooperative agreement with the National Science Foundation.

Djorgovski et al. 2000) and found to be a strongly lensed optical quasar (S. G. Djorgovski 2003, private communication). It was subsequently detected in hard X-ray (Vignali et al. 2005), FIR dust (Omont et al. 2001; Isaak et al. 2002), and radio continuum emission (Carilli et al. 2001), as well as molecular line emission (Cox et al. 2002; Carilli et al. 2002). It follows the radio-FIR correlation of star-forming galaxies (Carilli et al. 2001; Beelen et al. 2006), indicating that its FIR continuum emission is dominated by intense star formation. In spite of the fact that this source shows only two unresolved quasar images in the optical, previous CO observations have shown that the molecular gas reservoir in its host galaxy is lensed into an Einstein ring (Carilli et al. 2003, hereafter C03). These observations were also used to derive a first lensing model for this source. Based on the dynamical structure revealed by our new, higher resolution observations of PSS J2322+1944, we have developed a new lensing model, which enables us to reconstruct the velocity gradient in the spatially resolved gas reservoir. We use a concordance, flat ΛCDM cosmology throughout, with $H_0 = 71$ km s^{-1} Mpc^{-1}, $\Omega_M = 0.27$, and $\Omega_\Lambda = 0.73$ (Spergel et al. 2003, 2007).

2. OBSERVATIONS

We used the VLA in B configuration to observe the CO($J = 2 \rightarrow 1$) transition ($\nu_{\rm rest} = 230.53799$ GHz) toward PSS J2322+1944 between 2006 June 19 and July 3, and in C configuration between 2002 October 21 and November 15 (these short spacings data were published in the original study by C03). The total on-sky integration time in the 11 observing runs amounts to 70.5 hr. At $z = 4.119$, the line is redshifted to 45.0351 GHz (6.66 mm). Observations were performed in fast-switching mode (see, e.g., Carilli & Holdaway 1999) using the nearby source J23307+11003 for secondary amplitude and phase calibration. Observations were carried out under very good weather conditions with 26 or 27 antennas. The phase stability in all runs was excellent (typically $<20^\circ$ phase rms for the longest baselines). The phase coherence was checked by imaging a calibrator (J23207+05138) with the same calibration cycle as that used for the target source. For primary flux calibration, 3C 48 was observed during each run. Due to the restrictions of the VLA correlator, one 50 MHz intermediate frequency (IF) with seven 6.25 MHz channels was centered at the CO($J = 2 \rightarrow 1$) line frequency, leading to an effective bandwidth of 43.75 MHz (corresponding to 291 km s^{-1} at 45.0 GHz). This encompasses almost the full CO line width as measured in the CO($J = 5 \rightarrow 4$) transition ($\Delta v_{\rm FWHM} = 273 \pm 50$ km s^{-1}; Cox et al. 2002). Earlier observations set a 2 σ limit of 150 μJy on the continuum emission at the line frequency (Carilli et al. 2002).

For data reduction and analysis, the AIPS package was used. All data were mapped using the CLEAN algorithm and natural weighting. The synthesized clean beam using all data has a size of $0.33'' \times 0.30''$.[9] The final rms over a bandwidth of 37.5 MHz (250 km s^{-1}, excluding the noisy edge channel) is 48 μJy beam^{-1}. In addition, seven velocity channel maps (6.25 MHz or 42 km s^{-1} each) of the CO($J = 2 \rightarrow 1$) emission were created. The rms after Hanning smoothing is 77 μJy beam^{-1}. Convolving the data to a linear spatial resolution of $0.5''$ leads to slightly higher rms values of 49 and 80 μJy beam^{-1} for maps at 250 and 42 km s^{-1} velocity resolution, respectively.

[9] Imaging B configuration data only gives a resolution of $0.17'' \times 0.15''$ (natural weighting) or $0.12'' \times 0.11''$ (uniform weighting); however, most of the emission is outresolved in such maps.

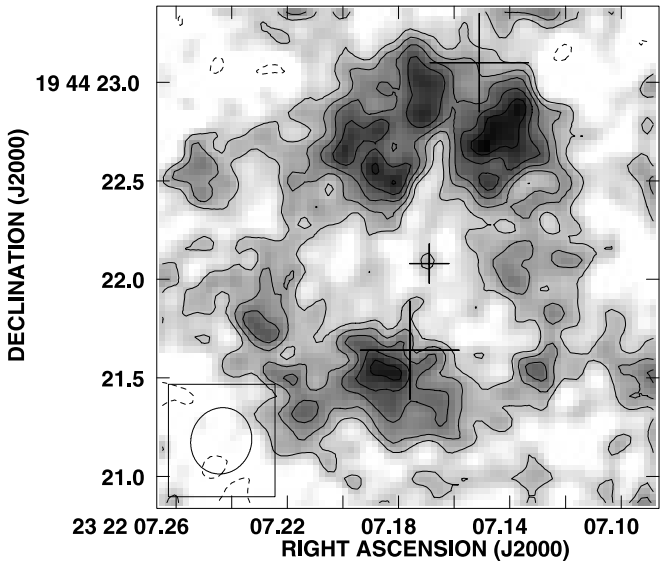

FIG. 1.—VLA map of the CO($J = 2 \rightarrow 1$) emission toward PSS J2322+1944 (integrated over the central 37.5 MHz, or 250 km s^{-1}). Contours are shown at -3, -2, 1, 2, 3, 4, and 5 σ (1 $\sigma = 48$ μJy beam^{-1}). The beam size ($0.33'' \times 0.30''$) is shown in the bottom left corner. The large crosses show the positions of the quasar images at $\lambda_{\rm obs} = 1.6$ μm ($\lambda_r = 314$ nm), and the small cross shows the position of the lensing galaxy at the same λ.

3. RESULTS

In Figure 1, the velocity-integrated CO($J = 2 \rightarrow 1$) emission over the central 250 km s^{-1} is shown. The emission is clearly resolved over multiple beams and extended on a scale of $\sim 1.5''$. The distribution of the gas is reminiscent of a full, almost circular molecular Einstein ring, consistent with previous indications of such a structure in lower resolution observations (C03). The emission varies in intensity along the ring, showing clear substructure.

The apparent surface brightness variations along the ring set strong constraints on the geometry of the lens configuration. The brightest CO peak on the ring can be used to set a lower limit on the intrinsic brightness temperature of the molecular gas. The peak strength of 280 ± 48 μJy beam^{-1} corresponds to a beam-averaged, rest-frame brightness temperature of $T_b = 8.7 \pm 1.5$ K. This is by a factor of a few lower than the kinetic gas temperature $T_{\rm kin}$ as predicted from CO line excitation models of this source (Riechers et al. 2006; Weiss et al. 2007; A. Weiss et al. 2008, in preparation) and indicates that the substructure of the molecular reservoir is not fully resolved by the observations.

We derive a spatially integrated CO($J = 2 \rightarrow 1$) line peak flux density of 2.50 ± 0.32 mJy, which is consistent with that found by Carilli et al. (2002). Assuming constant T_b between CO($J = 2 \rightarrow 1$) and CO($J = 1 \rightarrow 0$), and a CO luminosity to H_2 mass conversion factor for ultraluminous infrared galaxies [$\alpha = 0.8\,M_\odot$ (K km s^{-1} pc^2)$^{-1}$; Downes & Solomon 1998], this corresponds to a total molecular gas mass of $M(H_2) = 9.0 \times 10^{10} \mu_L^{-1}\,M_\odot$ (where μ_L is the lensing magnification factor, see below). Within the uncertainties, this is in agreement with the value found by Riechers et al. (2006) based on the CO($J = 1 \rightarrow 0$) luminosity.

To increase the peak signal-to-noise ratio, Figure 2 shows the CO($J = 2 \rightarrow 1$) emission convolved to $0.5''$ linear resolution. This contour map is shown overlaid on a gray-scale image of the (rest frame) 314 nm continuum emission of the source, as observed by the *Hubble Space Telescope* (*HST* NICMOS2 F160W; image adopted from Peng et al. 2006; C. Y. Peng 2008, private communication). The two brightest spots in the optical image

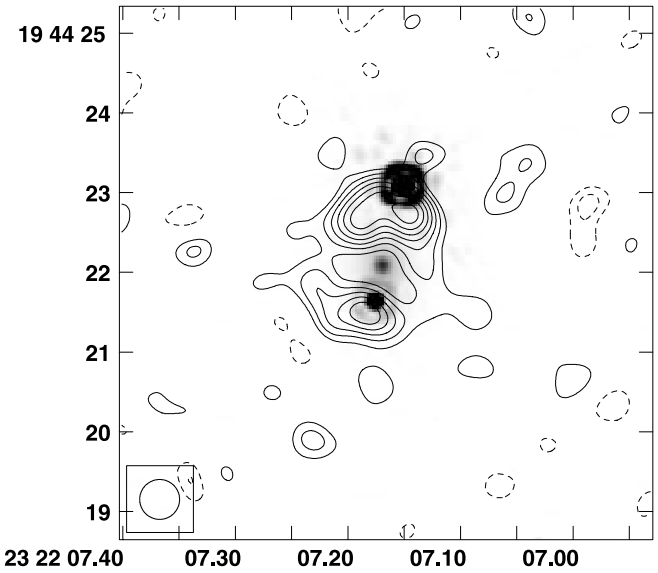

FIG. 2.—Contours of the CO($J = 2 \rightarrow 1$) emission as shown in Fig. 1, but convolved to a linear resolution of 0.5″ and overlaid on an *HST* NICMOS2 image at $\lambda_{obs} = 1.6$ μm (positions shown as crosses in Fig. 1). Contours are shown at -3, -2, 2, 3, 4, 5, 6, 7, and 8 σ (1 $\sigma = 49$ μJy beam^{-1}). Note that the *HST* image was not cleaned and thus shows Airy rings around the unresolved quasar images (Peng et al. 2006; C. Y. Peng 2008, private communication).

are unresolved lensed images of the AGN (henceforth "A" and "B,"[10] also indicated in Fig. 1, *large crosses*). The optical emission is likely dominated by the broad-line region of the AGN and thus expected to emerge from a compact circumnuclear parsec-scale region. The quasar images have a brightness ratio of $b(\mathrm{B, A}) = 0.181$. They coincide within 0.10″ with the positions measured by Keck at 430 nm (2.2 μm observed frame; C03), i.e., within the relative astrometric errors. These positions, however, are clearly offset from the brightest peaks of the molecular line emission. The third spot in the optical image is the lensing galaxy ("G," also indicated in Fig. 1, *small cross*). The lensing galaxy lies on the axis connecting images A and B, but by more than a factor of 2 closer to image B. However, it lies in the very center of the molecular Einstein ring, as expected. At the position of the lensing galaxy, we measure a 45.0 GHz radio continuum flux of 79 ± 47 μJy. This corresponds to only 1.7 σ and thus has to be considered tentative at best.

In the adopted cosmology, the optical brightness of PSS J2322+1944 corresponds to an apparent bolometric luminosity of $L_{bol} = 2.1 \times 10^{14} \mu_{L,opt}^{-1} L_{\odot}$ (Isaak et al. 2002). Assuming Eddington accretion, this corresponds to an apparent black hole mass of $M_{BH} = 7.0 \times 10^{9} \mu_{L,opt}^{-1} M_{\odot}$. Note that this may be considered a lower limit, as black holes in $z \sim 4$ quasars are found to have typical accretion rates of $\dot{M} = L_{bol}/L_{Edd} = 0.3$–$0.4$ (e.g., Shen et al. 2008).

In Figure 3, seven 42 km s^{-1} wide velocity channels of the CO($J = 2 \rightarrow 1$) emission line are shown (channel 7 was omitted from the data shown in Figs. 1 and 2 due to higher noise). Emission along the Einstein ring is detected in all channels. Clearly, the emission is moving systematically along the ring from the red part of the CO($J = 2 \rightarrow 1$) line to the blue. Note that there are many peaks of similar surface brightness (peak fluxes of 450–550 μJy beam^{-1}, or $T_b = 6$–7 K) that are found at different positions at different velocities. This indicates, to first order, a dynamical structure of uniform surface brightness, where the components at different velocities get projected to different positions in the lens plane. This puts us in the unique situation to model the gravitational lens configuration in this system in detail, and to recover the intrinsic dynamical structure of the quasar host galaxy in the background.

4. GRAVITATIONAL LENS INVERSION

In a previous attempt to model the gravitational lensing effect toward the molecular gas reservoir of PSS J2322+1944, C03 adopted a generic model based on the strongly lensed $z = 0.84$

[10] By convention, A is the brightest image.

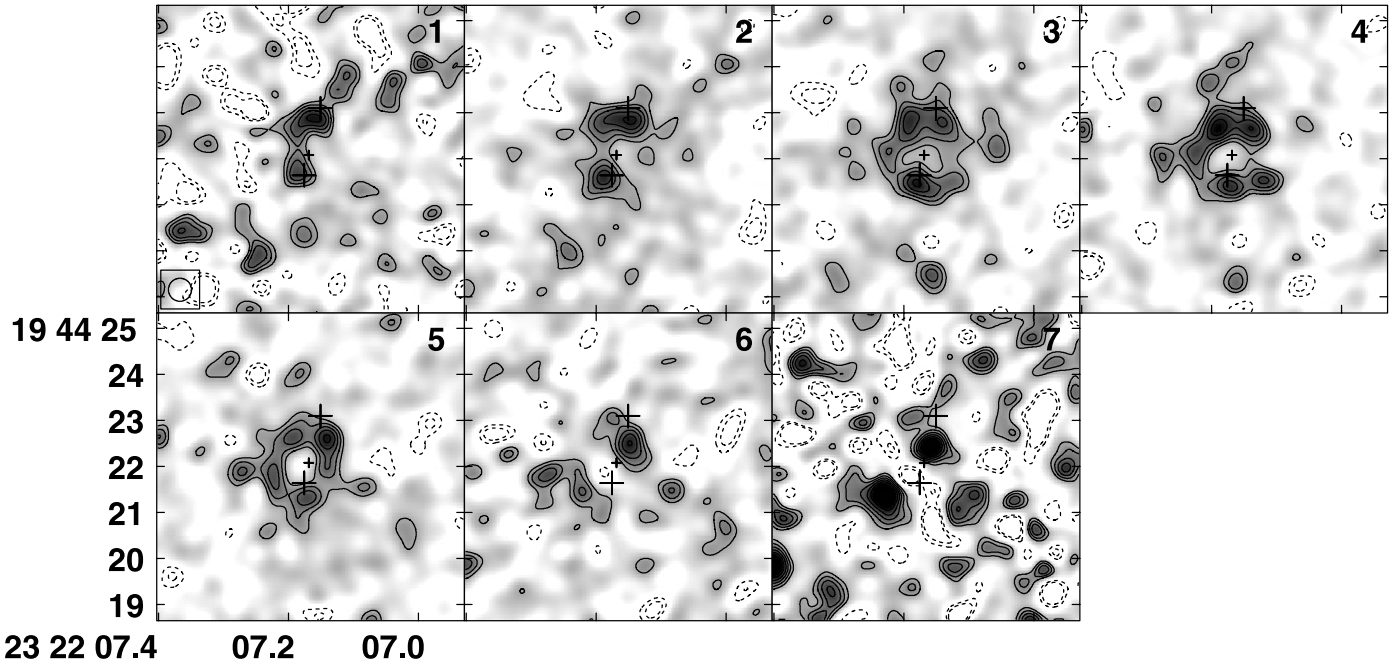

FIG. 3.—Channel maps of the CO($J = 2 \rightarrow 1$) emission at 0.5″ resolution (beam size is shown in the bottom left corner of the first panel). The same region is shown as in Fig. 2. One channel width is 6.25 MHz, or 42 km s^{-1} (frequencies increase with channel number and are shown at 45016.35, 45022.60, 45028.85, 45035.10, 45041.35, 45047.60, and 45053.85 MHz, redshifted to blueshifted). Contours are shown at -3, -2, 2, 3, 4, 5, and 6 σ (1 $\sigma = 80$ μJy beam^{-1}). Note that the noise in channel 7 is intrinsically higher by a factor of $\sqrt{2}$ relative to the other channels.

radio galaxy MG 1131+0456. By comparing various source configurations in the assumed lens potential and based on plausibility arguments, a model was found that described the overall properties of the observed ring structure. To enable us to describe the intrinsic properties of PSS J2322+1944 in more detail, we here present a direct model reconstruction and inversion of the lensing effect in this system. This modeling is based on the new CO observations presented in the previous section.

4.1. *Method: Bayesian Inference*

Due to the remaining observational uncertainties, it is not possible to derive a *unique* solution for the inversion of the gravitational lens. We thus explored the parameter space permitted by the data (and our modeling assumptions) to find the best possible solution; if some property of the models is consistent throughout this permitted volume, it can be considered well constrained at high confidence. This parameter study thus follows a Bayesian approach (Gregory 2005), using the Markov chain Monte Carlo (MCMC) code by Brewer & Lewis (2006a). This algorithm does not simply aim at minimizing χ^2 to find the best model (which may "overfit" the data by fitting part of the noise), but explores the whole range of plausible fits. By doing this, we can use a large number of parameters (e.g., source pixel values) in our model without overfitting the noise (since a broad region in parameter space with higher χ^2 can outweigh a particular solution that has very low χ^2 if the volume of the parameter space near the very low χ^2 solution is very small).

The Bayesian analysis thus encodes the phase space of possible source distributions allowed by the data into a probability distribution (e.g., Gregory 2005). The lensed image of the source was reconstructed based on the integrated CO emission line map and the structure detected in the velocity channels, and then used to derive a common model of the lensing galaxy's projected density profile that reproduces the emission in all channels simultaneously. Due to the differential structure among the velocity channels, this implies that the reconstructed source components after lens inversion will be different for each velocity channel and will reproduce the velocity gradient across the source.

In this model description, the unknowns to be inferred from the data are the seven source profiles $\{s_i\}_{i=1}^{7}$, one for each velocity channel, where s_i is shorthand for a large number of (unknown) pixel values. The unknown lens model parameters are denoted collectively by L. Given observed data D, the posterior distribution for the unknown parameters is proportional to the product of the prior distribution and the likelihood function:

$$p(\{s_i\}, L|D) \propto p(\{s_i\}, L)p(D|\{s_i\}, L). \quad (1)$$

Here D consists of seven extended images (one for each velocity channel). We make the following standard assumption for $p(D|\{s_i\}, L)$: Assuming that we know the source and lens properties, we would predict the observed image to be the lensed, blurred image of that source, plus additive Gaussian noise:

$$p(D|\{s_i\}, L) \propto \exp\left(-\frac{1}{2}\sum_{i=1}^{7}\chi_i^2\right), \quad (2)$$

where

$$\chi_i^2 = \sum_{j=1}^{N_{\rm pixels}}\left[\frac{D_{i,j} - M_j(s_i, L)}{\sigma_i}\right]^2. \quad (3)$$

Here $D_{i,j}$ is the jth pixel of the ith image, $M(s_i, L)$ is the model image calculated by lensing and blurring the ith source with the proposed lens model L, and σ_i is the noise standard deviation in the ith image estimated from the outer "blank sky" regions of each image, i.e., distant from any detected structure.

In this study, the lens was parameterized as a singular isothermal elliptical potential with five free parameters, which are the strength b of the lens, the ellipticity q of the potential, the central position (x_c, y_c) of the lensing source, and the angle of orientation θ of the projected density profile. For this model, the lensing potential is

$$\phi(x, y) = b\sqrt{qx'^2 + y'^2/q}, \quad (4)$$

where

$$\begin{pmatrix} x' \\ y' \end{pmatrix} = \begin{pmatrix} \cos\theta & \sin\theta \\ -\sin\theta & \cos\theta \end{pmatrix}\begin{pmatrix} x - x_c \\ y - y_c \end{pmatrix}. \quad (5)$$

The source plane position (x_s, y_s) corresponding to any lens plane position (x, y) is then given by the lens equation:

$$x_s = x - \frac{\partial\phi}{\partial x}, \qquad y_s = y - \frac{\partial\phi}{\partial y}. \quad (6)$$

The optical position of the lensing galaxy was *not* used as an initial model constraint to allow for a conservative treatment of the errors. However, the optical data are used in a second step to better constrain some of the source's intrinsic properties, as described in more detail below.

4.2. *Application to Interferometric Data*

Interferometer maps are reconstructed from visibility data using a scale that samples one synthesized interferometer beam (i.e., resolution element) with multiple pixels. This means that the noise is not independent for all pixels, as assumed by equation (3). Correct modeling of correlated noise is computationally very expensive and makes the evaluation of the likelihood (eq. [2]) very slow. In interferometric images, the scale of the synthesized beam, or point-spread function (PSF), usually is the same as the noise correlation scale (depending on the interferometer baseline weighting function used in the imaging Fourier transform). A good PSF model thus will allow for a proper, but faster, treatment of the noise properties.

The correlation length scale of the noise was measured at a clear distance from the detected molecular structure and used as the length scale for constructing an optimized Gaussian PSF. This length scale predicts that 1/62 of the pixels are effectively independent at the scale of the images ($0.03''$ pixel^{-1}). This corresponds to 106 pixels on the scale of the Einstein ring. To not "overfit" the image due to noise, only this fraction of information can be used to computationally determine the lens properties. This means that MCMC calculations have to be run at an "annealing temperature" of 62, or alternatively, the σ's can be artificially increased by a factor of $\sqrt{62}$ (e.g., Gregory 2005). The validity of this shortcut procedure was confirmed by ensuring that the residuals of the model images have the same statistical properties as the background in the observed maps.

4.3. *Priors*

The prior distribution for the lens parameters is chosen to be diffuse, but the final result is independent from this selection. For the seven unknown sources representing the source distribution in the velocity channels, we use independent "massive inference" priors (Brewer & Lewis 2006b). To generate a random source, a moderate number of "atoms" of a certain brightness are added to a blank source plane. These atoms are given a uniform probability distribution in position and an exponential probability distribution in flux. The width of each atom in pixels is chosen at random from one of three values to allow for the expectation that pixel values should be correlated with their neighbors. This procedure generates a random source in which most pixels are dim and is a more appropriate prior for astronomical sources than most conventional regularizers (Brewer & Lewis 2006a).

4.4. *Modeling Results*

4.4.1. *Lens Parameters*

From the MCMC run, we find that the lens has a strength $b = 0.745'' \pm 0.014''$, an ellipticity $q = 0.969 \pm 0.014$, and a position ($x_c = 0.074'' \pm 0.024''; y_c = -0.109'' \pm 0.029''$) (coordinates are relative to the center of the model images at $\alpha = 23^{\rm h}22^{\rm m}07.176^{\rm s}$, $\delta = +19^\circ 44' 22.16''$). Due to the fact that $q \simeq 1$, the lens potential is close to circular, as is the projected lens density profile. Even though the observed position of the lens ($x_c^{\rm obs} = 0.105''$; $y_c^{\rm obs} = -0.080''$) was not taken as an input parameter, the model naturally reproduces its position within the errors. The posterior probability distribution for θ is bimodal; with a probability of 62% (38%), the angle of orientation of the potential is $\theta = 109.2^\circ \pm 7.1^\circ$ ($62.7^\circ \pm 6.5^\circ$). The lens parameters are well constrained by the molecular data alone, so the marginal posterior distributions are close to Gaussian (except for the bimodal θ-distribution, which is well approximated by a mixture of two Gaussians). Thus, all of the estimates and uncertainties quoted above are of the form (mean $\pm$ standard deviation).

The lensing model described above was derived based on the distribution of the lensed CO emission only to allow for a conservative treatment of the errors and to avoid a main systematic source of error: the remaining astrometric uncertainties between the optical and radio reference frames. The results of our study indicate that the optical position of the lens is reproduced well, and thus that the astrometric offset appears to be small. Due to the fact that gravitational lensing is achromatic, we thus can use the model derived based on the distribution of the lensed CO emission only to also constrain the intrinsic optical properties of the source. We also can use the positions of the lensed images of the quasar in the optical to further constrain the allowed parameter space, and to estimate the position of the AGN within the deprojected molecular gas reservoir.

Based on the sample of lenses that fit the molecular line data, the optical positions of the quasar were ray-traced back into the source plane. As the optical emission of the source is compact, only those models that map both quasar images onto the same position in the source plane within the errors can be considered valid. We thus discarded all models that did not fulfill this extra criterion.

We find that this extra constraint only marginally changes previous results for the strength, ellipticity, and position of the lens. However, it does impact the solution for the angle of orientation of the potential and supports $\theta \sim 109^\circ$. As the source reconstructions presented in this section are not strongly sensitive to the extra constraint, only results (and the more conservative errors implied) from simulations produced without using the optical data are shown unless stated otherwise.

4.4.2. *Source Profiles*

For the seven source profiles in the different velocity channels, a "best" estimate was obtained by taking the average of all sources encountered by the MCMC run. This gives the posterior mean for each source, which is an optimal estimate, as it minimizes the expected squared error. As no unique solution exists for the lens inversion, the full source sample has a certain diversity. However, by taking the mean, only reproducible features are retained from the full sample. Due to the fact that both the resolution and sensitivity of the observations are finite, the resulting surface brightness profiles are expected to be smooth on a certain critical scale. Substructure may appear on smaller scales, but will be smoothed out in the final model due to the larger uncertainties involved in reproducing such small structures across the permitted volume in parameter space.

In Figure 4, the model-reconstructed (posterior mean) molecular gas distribution in the seven CO velocity channels (*columns*) are shown in the lens plane (*middle row*) and after lens inversion (*top row*), together with the observations (not convolved, i.e., at full spatial resolution; *bottom row*). Since the lens model is common to all velocity channels, the changing distribution of molecular gas between the velocity channels is due to intrinsic velocity structure in the background source (note the difference in scale between the lensed and the unlensed source).

In Figure 5, a color composite map of the modeled distribution of the CO in the velocity channels is shown. Orange corresponds to the redshifted part of the emission line, green corresponds to the central part, and blue corresponds to the blueshifted part. The image in the lens plane is displayed in the right panel, and the image in the source plane is shown after lens inversion in the left panel. A clear velocity gradient is seen in both images. The brightest part of the emission shows a systemic velocity structure that would be in agreement with a highly inclined, almost edge-on rotating disk of $\sim$2.5 kpc radius within the uncertainties of the data and modeling. This structure encloses a dynamical mass of $M_{\rm dyn} = 4.4 \times 10^{10} \sin^{-2} i \; M_\odot$ (assuming a line width of 273 km s^{-1} as given above), corresponding to only 2.5 times the lensing-corrected molecular gas mass (for highly inclined dynamical structures). However, there is also indication for a second, possibly tidal component (blue/green). This structure is slightly bent and also has an extent of almost 5 kpc, similar to the brighter component. Each component extends over at least 4–5 resolution elements in the source plane and thus is clearly detected and resolved.

The remaining uncertainties in the source reconstruction can be quantified by examining individual MCMC samples to calculate a probabilistic description of different properties of the source. A manual comparison of models considered to be "good" by our statistical analysis, however, shows that all share the same principal features, and only show significant differences in substructure on scales that are close to the resolution and detection limit, as expected. It thus is plausible that the overall structure and velocity gradient along the reconstructed source are real.

To quantify the uncertainties in the structure of the molecular gas reservoir of PSS J2322+1944 in the source plane, the posterior probability P that the flux in each pixel is nonzero is shown in Figure 6. The detection probability is shown over the full velocity range (i.e., summed up over all velocity channels). Due to the fact that observational data contain noise (i.e., finite positive or negative flux in every pixel of any velocity channel), the detection probability is nonzero in every pixel. Thus, a detection

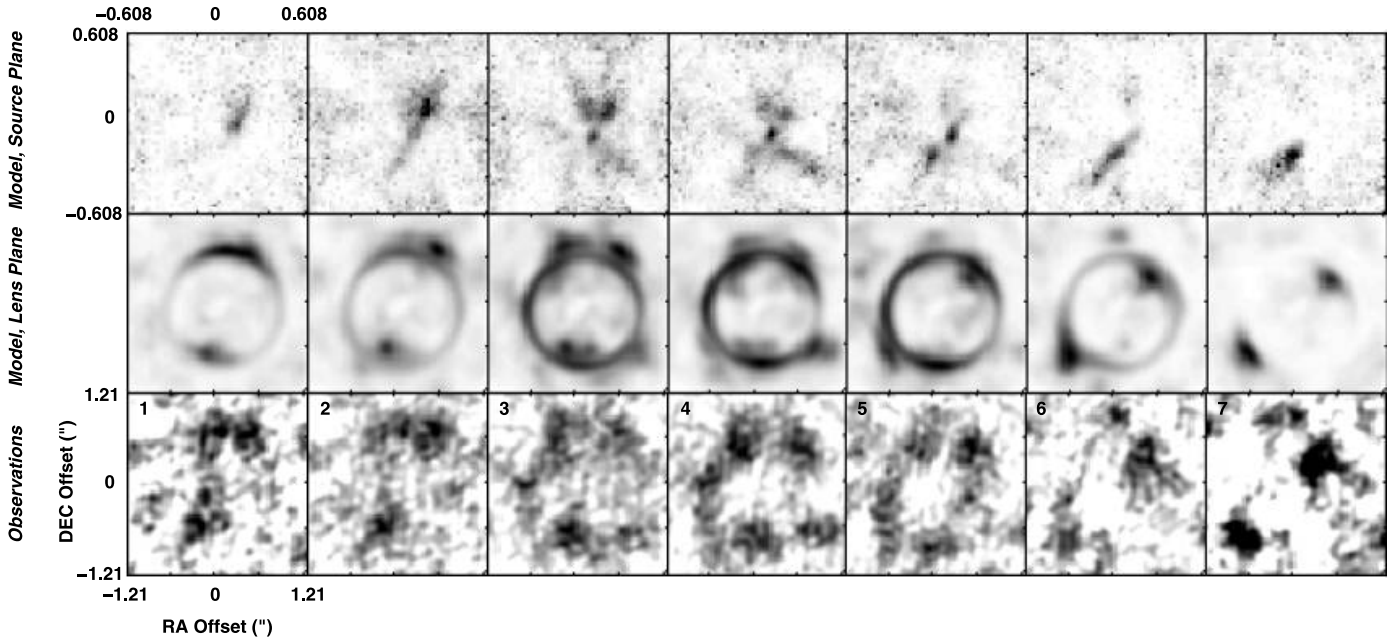

FIG. 4.—Reconstructed model images (posterior mean) of the 42 km s^{-1} CO($J = 2 \rightarrow 1$) velocity channels, and source morphologies after lens inversion. The bottom row shows the observed CO($J = 2 \rightarrow 1$) emission in the velocity channels as shown in Fig. 3, but without applying a beam convolution (i.e., same resolution as in Fig. 1, thus 1 $\sigma = 77$ μJy beam^{-1}). The middle row shows the model-reconstructed images of the channel maps in the lens plane (same scale as the bottom row). The top row shows the reconstructed images in the source plane after lens inversion. To account for the magnification of physical scales (and thus in effective spatial resolution), the model reconstruction in the source plane (same region as shown in Fig. 6; scale in arcseconds given on top) is shown zoomed in by a factor of 2 relative to the lens plane.

probability below a certain threshold has to be considered "background." The detection probability is consistently significantly higher than the background along the structures predicted by the "best model" (see Figs. 4 and 5).

The overall lensing magnification of the CO emission as predicted by the posterior distribution for the lens model is $\mu_L = 5.34 \pm 0.34$. Figure 7 shows the differential flux magnification between the velocity channels, estimated by calculating flux(lensed image)/flux(source) for the MCMC samples of each velocity channel. Although consistent with unity within the modeling uncertainties, there is tentative evidence that the flux is more gravitationally enhanced in the line center than in the outer channels. If real, this would suggest that the profile of the CO($J = 2 \rightarrow 1$) emission line is distorted by the lensing effect.

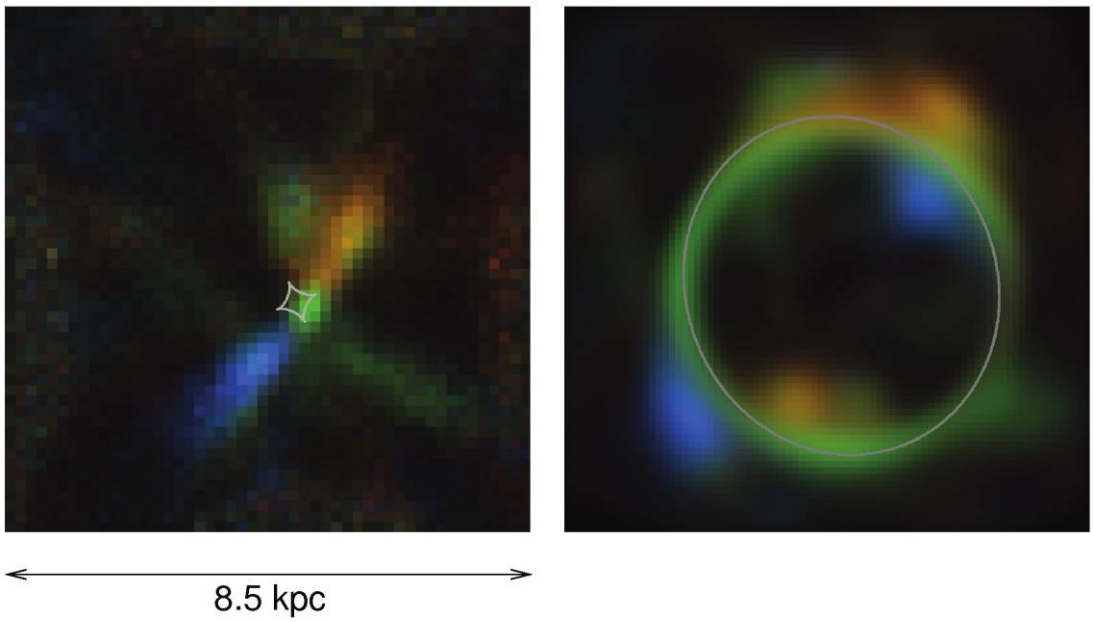

FIG. 5.—RGB composite color map of the model-reconstructed CO($J = 2 \rightarrow 1$) velocity channels shown in Fig. 4, with three colors encoding the velocity range of the emission (*orange*, redshifted [channels 1–2]; *green*, central [channels 3–5]; *blue*, blueshifted [channels 6–7]). The gray lines indicate the caustics. The bar at the bottom indicates the scale in the source plane. *Right*: Lensed, blurred image of the Einstein ring in the lens plane. *Left*: Image of the model-reconstructed quasar host galaxy in the source plane.

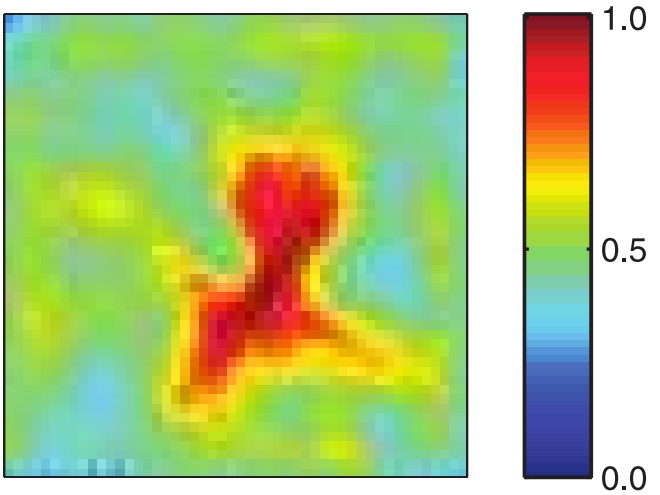

FIG. 6.—Map of the detection probability $P(\text{pixel} > 0)$ in the source plane after lens inversion, as derived from the full MCMC parameter study. A region of $1.21'' \times 1.21''$ size is shown.

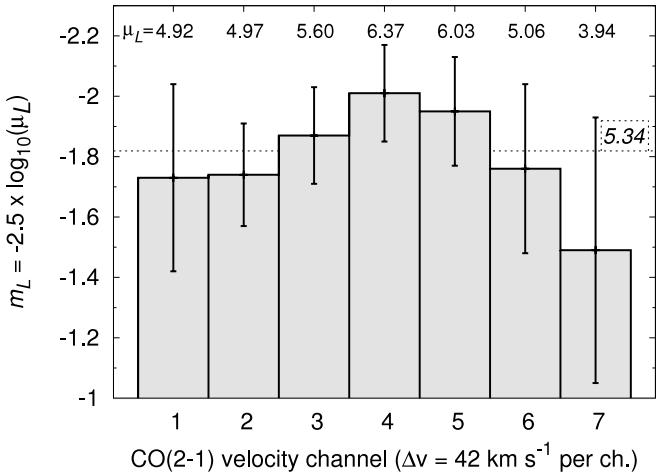

FIG. 7.—Model-predicted differential gravitational magnification between the CO velocity channels shown in Figs. 3 and 4. The magnification is shown in magnitudes (i.e., no magnification corresponds to $m_L = 0$). The error bars include the modeling uncertainties. The numbers on top indicate the magnification in each velocity channel. The dashed line indicates the total magnification of $\mu_L = 5.34$ in the integrated emission line map. [*See the electronic edition of the Journal for a color version of this figure.*]

The model-predicted lensing magnification of the 314 nm continuum emission from the AGN as derived from models based on both optical and CO data is $\mu_L^{\rm opt} = 4.7 \pm 0.4$. Excluding the optical constraints would result in slightly larger errors: $\mu_L^{\rm opt} = 4.8 \pm 0.6$. The overlay in Figure 2 suggests that the optical AGN is offset from the peak position of the molecular line emission. In the red CO line wing, the northern peak of the Einstein ring is brighter (as is the case for the two optical images), while in the blue line wing, the southern peak is brighter. This, together with the optical quasar image positions relative to the lens position, suggests that the AGN is located close to the orange peak of the reconstructed molecular gas distribution shown in Figure 5. This finding is supported by the model-based inversion of the optical and CO data, although the determination of the exact location within that part of the molecular structure is limited by the remaining model uncertainties and the limited accuracy of the relative astrometry of the optical and radio data. If the AGN is indeed located in the upper part of the disklike structure rather than in the center, one may speculate that the spatial and velocity structure of the reconstructed source is more likely to be due to interaction than to a rotating disk.

5. DISCUSSION

We have imaged and modeled a molecular Einstein ring of a galaxy at $z = 4.12$. Our high-resolution CO($J = 2 \rightarrow 1$) maps of the lensed quasar host galaxy of PSS J2322+1944 (a double-image optical quasar) reveal spatially resolved structure that shows a clear velocity gradient in the CO emission line. By performing a model-based lens inversion of the Einstein ring that is consistent with the data, we are able to reconstruct the velocity structure of this distant quasar host galaxy. The gravitational lensing effect acts as a natural telescope and allows us to zoom in on the molecular gas reservoir down to linear scales of only $\lesssim$1 kpc, sufficient to reveal velocity structure over almost 10 resolution elements in the source plane. Our novel modeling of this system reveals how the molecular gas crosses the central caustic (causing the appearance of the Einstein ring) moving from the redshifted to the blueshifted molecular emission. We also find evidence that the optical quasar may be associated with the redshifted part of the molecular reservoir. The full reservoir has a mass of $M(\rm H_2) = 1.7 \times 10^{10}\ M_\odot$ (corrected for lensing magnification). The molecular gas mass alone could account for almost half of the dynamical mass in this system if the galaxy were to be seen close to edge-on [$M_{\rm dyn} \sin^2 i / M(\rm H_2) \simeq 2.5$]. Due to the large spatial extent of the CO emission, and due to the fact that the AGN is probably largely offset from the center of the reservoir, we conclude that the molecular gas and dust are likely dominantly heated by star formation.

From the FIR luminosity of the source in the adopted cosmology ($L_{\rm FIR} = 2.4 \times 10^{13} \mu_L^{-1}\ L_\odot$; Cox et al. 2002), we derive a star formation rate[11] (SFR) of 680 $M_\odot\ {\rm yr}^{-1}$. At least part of the CO emission of the reconstructed source does not appear to follow a systemic trend in velocity. In this picture, this structure may be due to interaction, possibly caused by a major merger. Such an event could both feed the AGN and fuel the starburst and thus be responsible for the coeval assembly of a supermassive black hole and the stellar bulge in this system. Future observations of the FIR continuum at comparable spatial resolution may shed more light on this situation.

Motivated by these results, we can use the dynamical mass derived from the molecular line observations in the host galaxy of the $z = 4.12$ quasar PSS J2322+1944 in an attempt to constrain the relationship between the central SMBH mass and the stellar bulge mass ($M_{\rm BH}$-$M_{\rm bulge}$) in high-z AGN galaxies. Such a relation has been proposed for different types of galaxies in the local universe and appears to hold over more than 3 orders of magnitude in SMBH mass, essentially independent of galaxy type (predicting $M_{\rm bulge} \simeq 700 M_{\rm BH}$; see, e.g., Kormendy & Gebhardt 2001). Assuming the optical lensing factor of $\mu_L^{\rm opt} = 4.7$ derived from our model of PSS J2322+1944 and the Eddington limit derived in § 3 gives $M_{\rm BH} = 1.5 \times 10^9\ M_\odot$. With the further assumption that the dynamical molecular structure is seen close to edge-on, and that it traces a major fraction of the gravitational potential that hosts the stellar bulge, we thus find that $M_{\rm bulge} \simeq 30 M_{\rm BH}$ (subtracting out the black hole and gas masses would even give $M_{\rm bulge} < 20 M_{\rm BH}$). This value is by more than an order of magnitude offset from the local $M_{\rm BH}$-$M_{\rm bulge}$ relation, but in good agreement with results obtained for other high-z quasars, which

[11] We assume SFR $= 1.5 \times 10^{-10} L_{\rm FIR} (M_\odot\ {\rm yr}^{-1}\ L_\odot^{-1})$ (Kennicutt 1998). The dust temperature and spectral index of PSS J2322+1944 indicate that the FIR continuum emission is dominated by star formation, in agreement with the finding that the source follows the radio-FIR correlation for star-forming galaxies (Beelen et al. 2006).

show similar or larger offsets (e.g., Walter et al. 2004; Weiss et al. 2007; Riechers et al. 2008a, 2008b; see also Shields et al. 2006).

In the case of PSS J2322+1944, one may attempt to account for this offset by assuming that the dynamical structure is seen close to face-on (i.e., $i < 12^{\circ}$). This would, however, predict a large intrinsic CO line width ($\Delta v_{\rm FWHM} > 1300$ km s^{-1}). Such a line width would significantly exceed the velocity dispersions observed in the spheroids of massive present-day elliptical galaxies (which PSS J2322+1944 will likely evolve into) but is of the same order of magnitude as those observed toward some high-z submillimeter galaxies (e.g., Carilli & Wang 2006; Greve et al. 2005). Such large molecular line widths are consistent with those predicted by simulations of the hierarchical buildup of massive quasar host galaxies at high redshift (e.g., Narayanan et al. 2008) and thus compatible with the possible merger nature of PSS J2322+1944. However, in interacting or merging systems, molecular lines are likely more broad due to the fact that the dynamical molecular structure is not fully virialized yet. The molecular line widths in these galaxies thus may be by a factor of a few higher than the actual virial velocity of the host halo, which would lead to an overprediction of the bulge mass. It thus appears difficult to explain the offset from the local $M_{\rm BH}$-$M_{\rm bulge}$ relation by simply assuming a small inclination angle toward the line of sight. In addition, assuming that the AGN accretes at sub-Eddington rates, and/or taking into account that more than a third of the dynamical mass derived above is likely not stellar but accounted for by gas, dust ($<$1% of the gas mass), and the black hole, further increases this offset. Together with previous such examples, our results for PSS J2322+1944 thus appear to indicate that the black holes in massive galaxies at high redshift assemble earlier than a large fraction of their stellar bulges.

The observations and modeling presented herein demonstrate the power of spatially and dynamically resolved molecular gas studies in strongly lensed, distant AGN-starburst systems to provide direct evidence for the scenarios of quasar activity and galaxy assembly in the early universe as suggested by recent cosmological simulations (e.g., Springel et al. 2005). The boost in line intensity and spatial resolution provided by Einstein ring lens configurations are currently the only means by which to probe the dynamical structure of the most distant star-forming galaxies at (sub)kiloparsec resolution. Such observations provide an important foundation for future observations of molecular gas and dust in the early universe with the Atacama Large Millimeter/Submillimeter Array (ALMA), which will be able to probe more typical galaxy populations at high redshift to comparable and higher physical resolution, even without the aid of gravitational lensing.

The authors would like to thank Dennis Downes for helpful discussions and Chien Y. Peng for providing an *HST* image of PSS J2322+1944. D. R. acknowledges support from the Deutsche Forschungsgemeinschaft (DFG) through Priority Program 1177 and from NASA through Hubble Fellowship grant HST-HF-01212.01-A awarded by the Space Telescope Science Institute, which is operated by the Association of Universities for Research in Astronomy, Inc., for NASA, under contract NAS5-26555. C. C. acknowledges support from the Max-Planck-Gesellschaft and the Alexander von Humboldt-Stiftung through the Max-Planck-Forschungspreis 2005. We thank the anonymous referee for a thorough reading of the manuscript.

REFERENCES

Beelen, A., Cox, P., Benford, D. J., Dowell, C. D., Kovács, A., Bertoldi, F., Omont, A., & Carilli, C. L. 2006, ApJ, 642, 694
Brewer, B. J., & Lewis, G. F. 2006a, ApJ, 637, 608
———. 2006b, ApJ, 651, 8
Carilli, C. L., Bertoldi, F., Omont, A., Cox, P., McMahon, R. G., & Isaak, K. G. 2001, AJ, 122, 1679
Carilli, C. L., & Holdaway, M. A. 1999, Radio Sci., 34, 817
Carilli, C. L., Lewis, G. F., Djorgovski, S. G., Mahabal, A., Cox, P., Bertoldi, F., & Omont, A. 2003, Science, 300, 773 (C03)
Carilli, C. L., & Wang, R. 2006, AJ, 131, 2763
Carilli, C. L., et al. 2002, ApJ, 575, 145
Cox, P., et al. 2002, A&A, 387, 406
Djorgovski, S. G., et al. 2000, BAAS, 32, 1600
Downes, D., & Solomon, P. M. 1998, ApJ, 507, 615
Ferrarese, L., & Merritt, D. 2000, ApJ, 539, L9
Gebhardt, K., et al. 2000, ApJ, 539, L13
Graham, A. W., Erwin, P., Caon, N., & Trujillo, I. 2001, ApJ, 563, L11
Gregory, P. C. 2005, Bayesian Logical Data Analysis for the Physical Sciences: A Comparative Approach with Mathematica Support (Cambridge: Cambridge Univ. Press)
Greve, T. R., et al. 2005, MNRAS, 359, 1165
Guilloteau, S., Omont, A., Cox, P., McMahon, R. G., & Petitjean, P. 1999, A&A, 349, 363
Isaak, K. G., Priddey, R. S., McMahon, R. G., Omont, A., Peroux, C., Sharp, R. G., & Withington, S. 2002, MNRAS, 329, 149
Kennicutt, R. C., Jr. 1998, ApJ, 498, 541
Kormendy, J., & Gebhardt, K. 2001, in AIP Conf. Proc. 586, 20th Texas Symposium on Relativistic Astrophysics, ed. J. C. Wheeler & H. Martel (Melville: AIP), 363
Magorrian, J., et al. 1998, AJ, 115, 2285
Narayanan, D., et al. 2008, ApJS, 174, 13
Omont, A., Cox, P., Bertoldi, F., McMahon, R. G., Carilli, C., & Isaak, K. G. 2001, A&A, 374, 371
Peng, C. Y., Impey, C. D., Rix, H.-W., Kochanek, C. S., Keeton, C. R., Falco, E. E., Lehár, J., & McLeod, B. A. 2006, ApJ, 649, 616
Riechers, D. A., Walter, F., Carilli, C. L., Bertoldi, F., & Momjian, E. 2008a, ApJ, 686, L9
Riechers, D. A., Walter, F., Carilli, C. L., & Lewis, G. F. 2008b, ApJ, in press (arXiv:0809.0754)
Riechers, D. A., et al. 2006, ApJ, 650, 604
Shen, Y., Greene, J. E., Strauss, M. A., Richards, G. T., & Schneider, D. P. 2008, ApJ, 680, 169
Shields, G. A., Menezes, K. L., Massart, C. A., & Vanden Bout, P. 2006, ApJ, 641, 683
Solomon, P. M., & Vanden Bout, P. A. 2005, ARA&A, 43, 677
Spergel, D. N., et al. 2003, ApJS, 148, 175
———. 2007, ApJS, 170, 377
Springel, V., Di Matteo, T., & Hernquist, L. 2005, MNRAS, 361, 776
Vignali, C., Brandt, W. N., Schneider, D. P., & Kaspi, S. 2005, AJ, 129, 2519
Walter, F., Carilli, C., Bertoldi, F., Menten, K., Cox, P., Lo, K. Y., Fan, X., & Strauss, M. A. 2004, ApJ, 615, L17
Wang, R., et al. 2008, AJ, 135, 1201
Weiss, A., Downes, D., Neri, R., Walter, F., Henkel, C., Wilner, D. J., Wagg, J., & Wiklind, T. 2007, A&A, 467, 955
Weiss, A., Downes, D., Walter, F., & Henkel, C. 2007, in ASP Conf. Ser. 375, From Z-Machines to ALMA, ed. A. J. Baker et al. (San Francisco: ASP), 25